Research Article Vol. 25, No. 17 | 21 Aug 2017 | OPTICS EXPRESS 20202

Optics EXPRESS

Optical and electrical trade-offs of rib-to-contact distance in depletion-type ring modulators

SAMIRA KARIMELAHI,[1,*] WAHID RAHMAN,[1] MAHDI PARVIZI,[2] NAIM BEN-HAMIDA,[2] AND ALI SHEIKHOLESLAMI[1]

[1] *Department of Electrical and Computer Engineering, University of Toronto 10 King's College Road, Toronto, Ontario M5S 3G4, Canada*
[2] *Ciena, 3500 Carling Ave, Ottawa, Ontario K2H 8E9, Canada*
[*] *samira@ece.utoronto.ca*

Abstract: We present a study on electrical and optical trade-offs of the doping map in a ring modulator. Here, we investigate the effects of the high-doped region distance to edge of the waveguide sidewall. Four groups of ring modulators with different rib-to-contact distances are fabricated and measured where the key parameters such as extinction ratio, insertion loss, transmission penalty, and bandwidth are compared quantitatively. Small-signal responses for the selected ring modulators are simulated where results are in agreement with measurement results. We show that, at 4dB extinction ratio, decreasing the high-doped region distance to rib from 800nm to 350nm will increase the bandwidth by 3.8×. However, we observed 8.4dB increase the insertion loss. We also show that the high-doped region location affects the trade-off between bandwidth and frequency response magnitude at low frequencies. At 350nm, this trade-off is 2.5× and 3.8× more efficient compared to 550nm and 800nm, respectively.

© 2017 Optical Society of America

OCIS codes: (130.4110) Modulators; (230.0250) Optoelectronics; (230.5750) Resonators; (230.7370) Waveguides.

References and links

1. G. Li, X. Zheng, J. Yao, H. Thacker, I. Shubin, Y. Luo, K. Raj, J. E. Cunningham, and A. V. Krishnamoorthy, "25Gb/s 1V-driving CMOS ring modulator with integrated thermal tuning," Opt. Express **19**(21), 20435–20443 (2011).
2. X. Zheng, F. Liu, J. Lexau, D. Patil, G. Li, Y. Luo, H. Thacker, I. Shubin, J. Yao, K. Raj, R. Ho, J.E. Cunningham, A.V. Krishnamoorthy, , "Ultralow power 80 Gb/s arrayed CMOS silicon photonic transceivers for WDM optical links," J Lightwave Technol. **30**(4), 641–650 (2012).
3. M. Pantouvaki, P. Verheyen, G. Lepage, J. De Coster, H. Yu, P. De Heyn, A. Masood, W. Bogaerts, P. Absil, and J. Van Campenhout, "8 × 14Gb/s Si ring WDM modulator array with integrated tungsten heaters and Ge monitor photodetectors," in Optical Fiber Communications Conference and Exhibition (OFC) (2014), 1–3.
4. H. Li, Z. Xuan, A. Titriku, C. Li, K. Yu, B. Wang, A. Shafik, N. Qi, Y. Liu, R. Ding, T. Baehr-Jones, M. Fiorentino, M. Hochberg, S. Palermo, P. Y.Chiang, "22.6 A 25Gb/s 4.4 V-swing AC-coupled Si-photonic microring transmitter with 2-tap asymmetric FFE and dynamic thermal tuning in 65nm CMOS," in IEEE International Solid-State Circuits Conference-(ISSCC), 2015 , 1–3.
5. T. Y. Liow, K. W. Ang, Q. Fang, J. F. Song, Y. Z. Xiong, M. B. Yu, G. Q. Lo, and D. L. Kwong, "Silicon modulators and germanium photodetectors on SOI: monolithic integration, compatibility, and performance optimization," IEEE J. Sel. Top. Quantum Electron. **16** (1), 307–315 (2010).
6. S. J. Spector, C. M. Sorace, M. W. Geis, M. E. Grein, J. U. Yoon, T. M. Lyszczarz, E. P. Ippen, and F. X. Kartner, "Operation and optimization of silicon-diode-based optical modulators," IEEE J. Sel. Top. Quantum Electron. **16** (1), 165–172 (2010).
7. D. Thomson, F. Gardes, J.-M. Fedeli, S. Zlatanovic, Y. Hu, B. Kuo, E. Myslivets, N. Alic, S. Radic, G. Mashanovich, and G. Reed, "50-Gb/s Silicon Optical Modulator," IEEE Photon. Technol. Lett. **24**, 234–236 (2012).
8. J. Ding, H. Chen, L. Yang, L. Zhang, R. Ji, Y. Tian, W. Zhu, Y. Lu, P. Zhou, R. Min, and M. Yu, "Ultra-low-power carrier-depletion Mach-Zehnder silicon optical modulator," Opt. Express **20**, 7081–7087 (2012).
9. D. Petousi, L. Zimmermann, A. Gajda, M. Kroh, K. Voigt, G. Winzer, B. Tillack, and K. Petermann, "Analysis of optical and electrical tradeoffs of traveling-wave depletion-type si mach–zehnder modulators for high-speed operation," IEEE J. Sel. Top. Quantum Electron. **21**(4), 1–8 (2015).
10. G. Li, A. V. Krishnamoorthy, I. Shubin, J. Yao, Y. Luo, H. Thacker, X. Zheng, K. Raj, and J. E. Cunningham, "Ring resonator modulators in silicon for interchip photonic links," IEEE J. Sel. Top. Quantum Electron. **19**(6), 95–113 (2013).
11. H. Jayatilleka, W. D. Sacher, and J. K. S. Poon, "Analytical model and fringing-field parasitics of carrier-depletion silicon-on-insulator optical modulation diodes," IEEE Photon. Technol. **5**(1), 2200211 (2013).

#291523 https://doi.org/10.1364/OE.25.020202
Journal © 2017 Received 29 Mar 2017; revised 23 Jul 2017; accepted 26 Jul 2017; published 11 Aug 2017

12. F. Y. Gardes, D. J. Thomson, N. G. Emerson, and G. T. Reed, "40 Gb/s silicon photonics modulator for TE and TM polarisations," Opt. Express **19**, 11804–11814 (2011).
13. W. D. Sacher and J. K. Poon, "Dynamics of microring resonator modulators," Opt. Express **16**(20), 15741–15753 (2008).
14. H. Yu, D. Ying, M. Pantouvaki, J. Van Campenhout, P. Absil, Y. Hao, J. Yang, and X. Jiang, "Trade-off between optical modulation amplitude and modulation bandwidth of silicon micro-ring modulators," Opt. Express **22**(12), 15178–15189 (2014).
15. J. Müller, F. Merget, S. S. Azadeh, J. Hauck, S. R. García, B. Shen, and J. Witzens, "Optical peaking enhancement in high-speed ring modulators," Sci. Rep. **4**, 6310 (2014).
16. J. Rhim, Y. Ban, B.-M. Yu, J.-M. Lee, and W.-Y. Choi, "Verilog-A behavioral model for resonance-modulated silicon micro-ring modulator," Opt. Express **23**(7), 8762–8772 (2015).
17. R. Dube-Demers, J. St-Yves, A. Bois, Q. Zhong, M. Caverley, Y. Wang, L. Chrostowski, S. LaRochelle, D. Plant, and W. Shi, "Analytical modeling of silicon microring and microdisk modulators with electrical and optical dynamics," J Lightwave Technol. **33**, 4240–4252 (2015).
18. S. Karimelahi and A. Sheikholeslami, "Ring modulator small-signal response," in Conference on Lasers and Electro-Optics, OSA Technical Digest (2016), paper JW2A.133.
19. Samira Karimelahi and Ali Sheikholeslami, "Ring modulator small-signal response analysis based on pole-zero representation," Opt. Express **24**, 7585–7599 (2016).
20. *http://www.ime.a-star.edu.sg/PPSSite/index.asp*.
21. R. A. Soref and B. R. Bennett, "Electrooptical effects in silicon," IEEE J. of Quant. Electron. **23**(1), 123–129 (1987).
22. L. Zhang, Y. Li, J.-Y. Yang, M. Song, R. G. Beausoleil, and A. E. Willner, "Silicon-based microring resonator modulators for intensity modulation," IEEE J. Sel. Top. Quantum Electron. **16**(1), 149–158 (2010).
23. J. K. S. Poon, J. Scheuer, S. Mookherjea, G. T. Paloczi, Y. Huang, and A. Yariv, "Matrix analysis of microring coupled-resonator optical waveguides," Opt. Express **12**, 90–103 (2004).
24. B. E. Little, S. T. Chu, H. A. Haus, J. Foresi, and J. P. Laine, "Microring resonator channel dropping filters," J Lightwave Technol. **15**, 998–1005 (1997).
25. T. Baehr-Jones, R. Ding, A. Ayazi, T. Pinguet, M. Streshinsky, N. Harris, J. Li, L. He, M. Gould, Y. Zhang, A. Eu-Jin Lim, T.Y. Liow, S. H. Teo, G. Q. Lo, M. Hochberg, "A 25 Gb/s silicon photonics platform," arXiv preprint arXiv:1203.0767 (2012).
26. *https://www.lumerical.com*.
27. M. Pantouvaki, P. Verheyen, G. Lepage, J. De Coster, H. Yu, P. De Heyn, P. Absil, and J. Van Campenhout, "20Gb/s silicon ring modulator co-integrated with a Ge monitor photodetector," in European Conference on Optical Communication (ECOC), 2013, 1-3.
28. Q. Xu, B. Schmidt, J. Shakya, and M. Lipson, "Cascaded silicon micro-ring modulators for WDM optical interconnection," Opt. Express **14**(20), 9431–9435 (2006).

---

1. Introduction

Data traffic is increasing mostly due to consumer usage via high data-demanding applications such as video streaming and cloud computing. One of the methods to increase the capacity of data communication on a single optical fiber is to use wavelength division multiplexing (WDM). One of the most desirable optical modulators in WDM links is the carrier-depletion silicon ring modulator employing a reverse-biased pn diode [1–4]. Therefore, the depletion-type ring modulator, a main building block in a WDM link, should be optimally designed. One of the main design parameters of the ring modulator is bandwidth which is partially affected by the design of the doped waveguide. Another important factor is the coupling condition of the ring modulator.

Several studies are done to optimize the waveguide geometry and doping profile of a pn doped waveguide [1,5–10]. It is shown that electrical bandwidth of the depletion-mode waveguide can be increased using the following methods: a higher dopant concentration for the p and n regions to reduce series resistance, a higher reverse bias voltage to decrease junction capacitance [9], a higher ratio of slab thickness to rib height [11], or a smaller distance between highly doped region, p_{++}/n_{++}, and the edge of the waveguide (d_{++}) to decrease series resistance [6, 11]. However, there are multiple trade-offs associated with each of these methods. Increasing the dopant concentration not only increases the optical loss, but also increases the junction capacitance. Therefore careful design of the dopant concentration is required [9, 10]. Moreover, available doping levels are usually limited to certain levels in each foundry when custom run

is not available. In terms of the waveguide geometry or bias voltage, higher bias voltages and higher ratios of slab thickness to rib height would result in a lower modulation efficiency [11]. The latter is due to the lower lateral mode confinement. It is theoretically predicted that one optimum way to increase bandwidth without sacrificing modulation efficiency is reducing the series resistance by decreasing d_{++} in reverse-biased pn diode waveguide [11]. However, too much reduction of d_{++} results in an increase in optical loss [11, 12]. This is due to optical mode lateral extension to the highly doped region [5] as well as the dopant diffusion to the waveguide during the annealing process. The latter increases the free carrier absorption. This additional loss is experimentally studied in IME A*Star process for a certain waveguide geometry [5]. However, the quantitative influences of decreasing d_{++} on the loss and bandwidth of ring modulator are little discussed. The main goal in many of the above studies is to optimize Mach-Zehnder modulator (MZM) bandwidth and modulation efficiency, and the results may not be applicable to ring modulators. This is due to the more complex nature of resonance in ring modulators which couples the optimization of optical and electrical parameters. As both the cavity photon lifetime and the electrical (i.e. the RC limited) bandwidth of carrier-depletion ring modulators are affected by d_{++}, and since d_{++} is not limited by the foundry, it can be used as a handle to further optimize ring modulator design. Hence, it is important to systematically study design trade-offs of d_{++}.

In this paper, we quantitatively study the impacts of decreasing d_{++} on the performance of reverse-biased ring modulators. Four groups of reverse-biased ring modulators with different values of d_{++} and coupling gaps are studied. The key performance parameters such as extinction ratio, modulator penalties, insertion loss, and ring modulator electrical and optical bandwidth are compared at various d_{++} values based on measurement and simulation results.

To accurately calculate the ring modulator bandwidth (f_{3dB}), small-signal analysis should be used. This is due to the fact that, in addition to optical (f_Q) and electrical (f_{RC}) bandwidths, carrier wavelength is also important as it may lead to resonance peaking in the frequency response [13–19]. Small-signal models of ring modulator have been studied previously [13–19] and can be used to evaluate the effect of various design parameters on ring modulator performance. In this paper, in addition to measurement, we use our small-signal model presented in [19] as a tool to study the effect of d_{++} on the frequency response of ring modulators which provides additional insight into frequency response trade-offs. Also, the rate of increase in bandwidth at the cost of decreasing DC value of the frequency response (DC gain) is calculated based on the electro-optical frequency response and compared across ring modulators with various d_{++}. We show that d_{++} can also be used as a tuning factor in changing the amount of trade-off between the frequency response DC gain and bandwidth. Finally, performance of each of these ring modulators is compared according to the device bandwidth, extinction ratio (ER), and insertion loss (IL).

2. Device description

To quantitatively assess the effects of d_{++} on the ring modulator performance, we characterize all-pass ring modulators fabricated in IME A*Star process [20]. Schematic of the ring modulator doped waveguide cross-section is shown in Fig. 1. Ring modulators are fabricated on a Silicon on Insulator (SOI) wafer with a top Si layer of 220nm and 2μm thick buried oxide layer. The slab thickness of the rib waveguide is 90nm. The doping concentration for low-doped region is $3 \times 10^{17} cm^{-3}$ for n and $5 \times 10^{17} cm^{-3}$ for p, and for high-doped contact region is $10^{20} cm^{-3}$. Note that the chosen doping concentrations may not be the optimum values, but rather those fixed concentrations offered by the foundry. The doped section is taking 75% of the ring circumference excluding the coupling region. As shown in Fig. 1, pn junction has 50nm offset from the waveguide center as holes induce less free carrier absorption loss and more refractive index change [21]. Twenty ring modulators in total are fabricated with various distances of

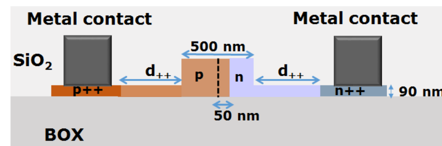

Fig. 1. Ring modulator waveguide cross-section.

the highly-doped region to the edge of the waveguide, d_{++}. These include four groups of ring modulators with d_{++} of 200nm, 350nm, 550nm, and 800nm. In each group, the gap between the ring modulator and the bus waveguide ranges from 200nm to 400nm with a step of 50nm to enable finding the ring modulator at or close to its critical coupling condition. Radius and waveguide widths of all the rings are 10μm and 500nm, respectively.

3. Device DC performance measurement and analysis

In order to identify ring modulators closest to the critical coupling condition in each group, static power transmission of all 20 ring modulators are measured when no DC voltage is applied. Grating couplers are used to couple the tunable laser source (Agilent 8164A) in and out of the chip to the optical power meter (N7744A). Coupling loss is around 5dB per grating. For each group of ring modulators, the notch depths of power transmission spectra are measured and plotted versus gap in Fig. 2(a) where data points are indicated with markers. The rising and falling trends in the notch depth indicate a transition in the coupling condition. For example, for d_{++} of 350nm and 550nm, it is clear that ring modulators before and after the maximum notch depth are in different coupling conditions. Amplitude decay time constant due to ring-to-bus waveguide coupling (τ_e) increases when the gap gets wider, whereas the other part of the amplitude decay time constant arising from intrinsic loss inside the cavity (τ_l) stays constant. As such, ring modulators with d_{++} of 350nm and 550nm can be classified in terms of their coupling conditions. However, modulators with the maximum notch depth need optical parameters to be extracted to verify their coupling conditions. Knowing that τ_l increases by increasing d_{++}, coupling conditions of the ring modulators with d_{++} of 200nm and 800nm are also determined. Figure 2(b) shows color-coded coupling conditions for each group of d_{++} where the over-coupled and under-coupled rings are shown in orange and blue, respectively. Also, data points are shown with cross markers. The boundary between under and over coupling conditions are shown with shaded colors as it is uncertain. According to Fig. 2(b), the critical coupling condition is not reached for $d_{++} = 200nm$, as loss is high and gap smaller than 200nm is required. In the other three groups of d_{++}, ring modulators closest to the critical coupling condition are selected for further analysis. In this study, it is important to pick rings close to the critical coupling condition as the coupling condition (i.e. deep under- or over-coupling) changes the dynamic response of the ring modulator [14,19,22]. Selected rings are indicated with circles in Fig. 2(b): Ring B with $d_{++} = 350nm$ and $gap = 250nm$, Ring C with $d_{++} = 550nm$ and $gap = 350nm$, and Ring D with $d_{++} = 800nm$ and $gap = 400nm$. In some comparison notes, for example ring loss, a ring modulator with $d_{++} = 200nm$ and $gap = 200nm$, referred to as Ring A, is also included.

Transmission spectra at through ports of the ring modulators A to D under reverse-biased conditions are shown in Figs. 3(a) and 3(d), respectively. Despite the same radius, due to the process variation on waveguide geometry (e.g. sidewall angle and waveguide width), the resonance wavelengths are different. For Ring A due to low quality factor, only the results for 0V and -4V are shown, while the results for 0V to -6V are plotted for Rings B-D. Notch-depth variation due to increasing bias voltage indicates Ring A to D are under-, under-

Optics EXPRESS

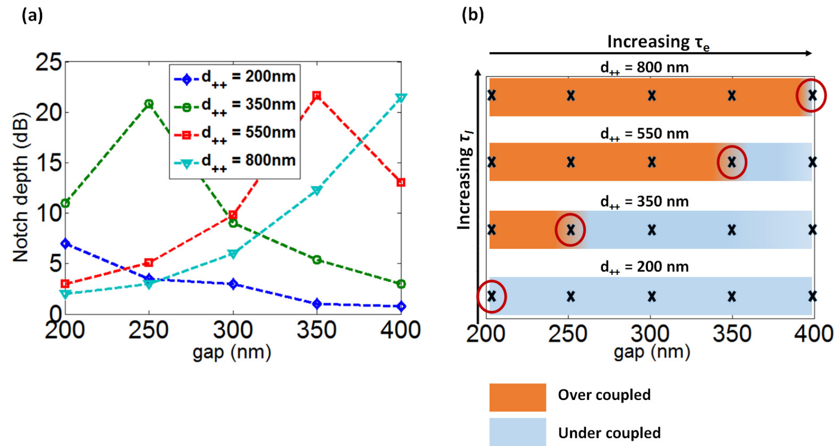

Fig. 2. (a) Notch depth versus gap. (b) Color-coded figure showing coupling conditions of the tested ring modulators.

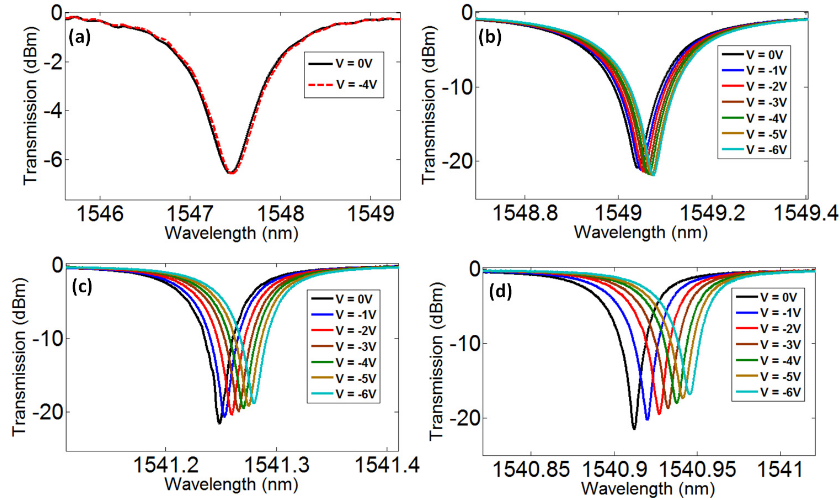

Fig. 3. Measured optical power transmission spectra at various bias voltages for (a) Ring A with $d_{++} = 200nm$, (b) Ring B with $d_{++} = 350nm$, (c) Ring C with $d_{++} = 550nm$, (d) Ring D with $d_{++} = 800nm$.

, over-, and over-coupled, respectively. Resonance wavelength shift of about 7-8pm/V is observed. In this work, the aim is not to optimize modulation efficiency, as the available doping concentrations are limited and low. Efficiency of 24pm/V could be achieved with about 10× higher concentration [1].

Optical parameters of the ring modulators are extracted by fitting the measured data to the ring static transmission formula of [23]:

$$H_s(\Delta\omega) = \frac{j\Delta\omega + \frac{1}{\tau} - \frac{2}{\tau_e}}{j\Delta\omega + \frac{1}{\tau}}, \tag{1}$$

where $\Delta\omega$ is angular frequency detuning with respect to the angular resonance frequency, τ is the electric field amplitude decay time constant and $1/\tau = 1/\tau_e + 1/\tau_l$ with τ_e and τ_l being

the amplitude decay time constants due to the intrinsic loss inside the cavity and due to the ring to bus waveguide coupling, respectively. Quality factor (Q), of the ring resonator is related to the decay time constant through $\tau\omega_{res}/2$ where ω_{res} is the angular resonance frequency. This means when the life time (decay time constant) of circulating light inside the ring resonator is higher, ring has higher quality factor.

Table 1 summarizes the key optical parameters of τ_l, τ_e, τ, cavity linewidth, Q, and the coupling condition for Rings B to D at -1V bias voltage. The parameters for Ring A at 0V are also added in this table for comparison. Group index, n_g, is extracted to be 3.86.

Table 1. Extracted optical parameters from the measured transmission spectra.

Ring	d_{++}(nm)	τ_l(ps)	τ_e(ps)	τ(ps)	Linewidth(pm)	Q	Coupling Condition
Ring A,@ 0V	200	3.4	9.6	2.5	742.2	2,084	Deep under-coupled
Ring B,@ -1V	350	14.7	17.7	8	314.4	4,971	Slightly under-coupled
Ring C,@ -1V	550	71.2	59.1	32.3	77.4	20,068	Slightly over-coupled
Ring D,@ -1V	800	124	101.5	55.8	44.8	34,627	Slightly over-coupled

According to the table, by decreasing d_{++} from 800nm in Ring D to 200nm in Ring A, τ_l decreases about 36× due to increase in optical losses. Decreasing d_{++} also lowers the ring quality factor which leads to a higher optical bandwidth. However, decreasing d_{++} too much (i.e. 200nm) results in the impractical device due to a very low quality factor ($Q = 2,084$ in Ring A).

From measured transmission spectra shown in Figs. 3(a) and 3(d), τ_l as a function of voltage is extracted and shown in Fig. 4(a) with circles for all four rings. Also shown in the solid line is the quadratic fit. Variation in τ_e over voltage is insignificant, as the coupling region is not doped. From the extracted voltage-dependent τ_l, the power loss coefficient in $1/m$ is calculated as [24]

$$\alpha = \frac{2}{v_g \tau_l}, \tag{2}$$

where v_g is the group velocity. Based on this, additional optical loss with respect to $d_{++} = 800nm$ is plotted in Fig. 4(b). Total optical loss for $d_{++} = 800nm$ is around 9dB/cm. This loss includes a propagation loss, which is reported to be around 2-3dB/cm in similar fabrication process [25], and radiation loss due to bending, which is expected to be around 2dB/cm from simulation using commercial software [26]. The rest is due to the doped waveguide. The additional loss shown in Fig. 4(b) is due to lateral mode expansion to the high-doped region. According to Fig. 4(b), this additional loss rises rapidly with decreasing d_{++} where, for example at $d_{++} = 550nm$ the additional loss of 6.6dB/cm increases to over 300dB/cm at $d_{++} = 200nm$. The increase of loss by decreasing d_{++} depends on the lateral confinement set by waveguide geometry such as the ratio of rib height to slab thickness [5].

Refractive index change with respect to 0V, Δn_{eff}, as a function of voltage is also determined and plotted (Fig. 4(c)) for Rings B-D based on the $\Delta n_{eff} = \frac{n_g \Delta\lambda_r}{F\lambda_r}$. Here, $\Delta\lambda_r/\lambda_r$ is the normalized resonance shift and F is the ratio of pn junction length to the ring circumference [10]. As expected, changing d_{++} does not alter modulation efficiency. Small changes observed in this figure may arise due to process variations from one ring to another.

In order to evaluate ring modulator performance based on the tested DC characteristics, static ER and IL are calculated from transmission spectra shown in Figs. 3(b) and 3(d), for Rings B-D assuming voltage swing from 0V to 3V. Figures 5(a) and 5(b) show ER and IL plots versus relative input wavelength to the resonance wavelength at 0V, respectively. Although all three rings are close to critical coupling, due to the lower quality factor of Ring B, the maximum achievable ER with 3V applied voltage is much smaller than Rings C and D, as shown in Fig 5(a). Also, due to the lower slope in the transmission spectra (wider transmission spectrum), the rate of

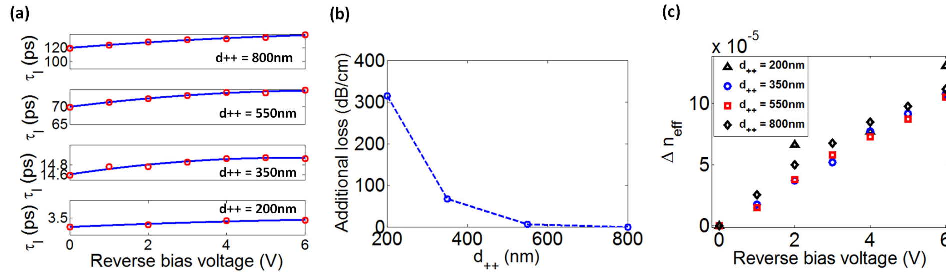

Fig. 4. (a) Extracted τ_l shown with markers for Rings A-D with d_{++} from 200nm to 800nm together with the fitted curves shown with solid lines. (b) Extracted additional loss as a function of d_{++}.(c) Extracted Δn_{eff} versus voltage for Rings A-D with d_{++} from 200nm to 800nm.

change in ER value versus relative wavelength is smaller when d_{++} is smaller. Moreover, the corresponding IL in Fig. 5(b) is higher for smaller d_{++}.

Another metric to evaluate the ring modulator performance is transmission penalty [27] defined as $T_p = -10log(\frac{P_1-P_0}{2P_{in}})$ where P_1 (P_0) is transmitted power at bit 1 (bit 0) and P_{in} is the input power. Transmission penalties for Ring B to D are shown in Fig. 5(c) where the minimum TP for Ring B and D are 14.8dB and 5.8dB, respectively. This means that the amount of optical modulation amplitude with respect to the input power decreases significantly when d_{++} is smaller. However, when a higher bandwidth is required, the relative wavelength should increase which will result in a rapid increase in TP for Rings C and D. The bandwidth dependency over working wavelength will be discussed in further details later in the paper.

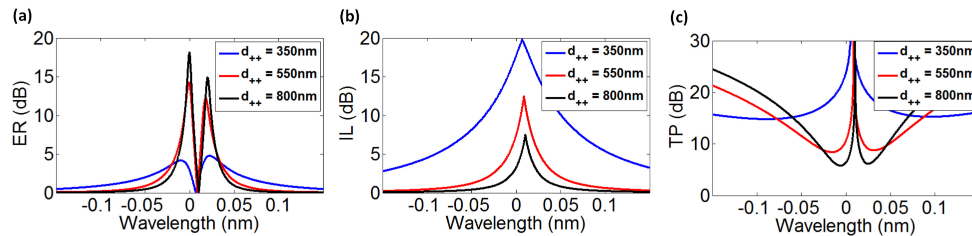

Fig. 5. (a) Extinction ratio (ER), (b) insertion loss (IL), and (c) transmission penalty (TP) for voltage swing from 0 to 3V. The plot for each ring is normalized to resonance wavelength of the corresponding ring.

In Figs. 6(a) and 6(b), the maximum ER (ER_{max}) and the corresponding IL as a function of applied voltage with respect to 0V (ΔV) are shown for Rings B-D. According to this, from 0V to 6V, ER_{max} increases from 1.6dB, 5.8dB, and 12dB to 8.8dB,17.8dB, and 20dB for Rings B-D, respectively. Also, from 0V to 6V, corresponding IL decreases from 17.4dB, 15dB, and 9.2dB to 12.4dB, 3.8dB, and 1.4dB for Rings B-D, respectively.

All these parameters are essential to designing functional ring modulators as will be discussed later in the discussion section.

4. Device small-signal characteristics

The small-signal electrical response of the ring modulator is modeled by the equivalent circuit shown in Fig. 7 [1]. Here, C_{pad}, C_j, and C_{ox} are the capacitance between the pads, the capacitance of the reverse-biased pn junction, and the capacitance through the oxide layer, respectively. Also, R_{sj} and R_{Si} are the series resistance of the pn junction and the resistance

Optics EXPRESS

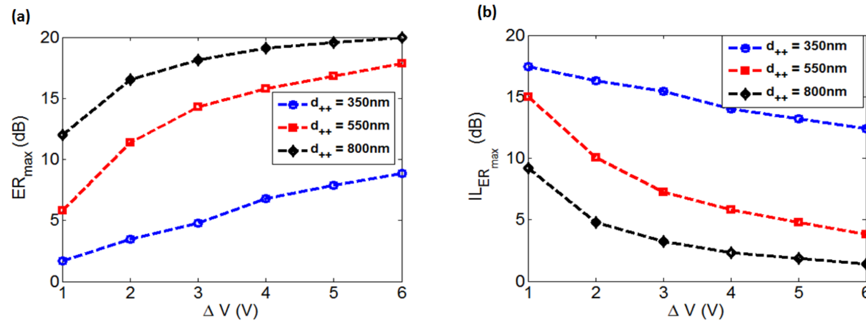

Fig. 6. (a) Measured maximum ER and (b) corresponding IL versus applied voltage.

of the Si substrate. The electrical circuit elements are extracted by fitting the simulated S_{11} coefficients of the equivalent circuit to the measured S_{11} magnitude and phase. Measured phase and magnitude of S_{11} for Ring D at -1V bias voltage are shown in Figs. 8(a) and 8(b), respectively. Also shown in dashed lines is S_{11} simulated by ADS assuming 50Ω source resistor. The extracted circuit elements are $C_{ox} = 10fF$, $R_{Si} = 30k\Omega$, $C_{pad} = 2fF$, $C_j = 12fF$, and $R_{sj} = 208\Omega$. S_{11} for Rings B and C are also measured, but are not presented here for brevity. The circuit element which varies by changing d_{++} is R_{sj}. Other extracted circuit components stay almost similar where the maximum variation in C_j is about $1fF$. The value of R_{sj} for Rings B and C are extracted to be 125Ω and 154Ω, respectively. R_{sj} and C_j are also calculated based on the methods presented in [17] to be 211Ω for Ring D, 160Ω for Ring C, and 110Ω for Ring B and around $11.7fF$. These values are in agreement with the measured results. Small deviations are attributed to process variation. Considering a 50Ω source impedance, f_{RC} for Rings B, C, and D are computed at -1V to be 75GHz, 59GHz, and 51GHz which are 2×, 6×, and 9× larger than their f_Q, where f_Q is defined as $1/\pi\tau$, respectively. This suggests that f_Q is the main limiting factor in bandwidth for all three rings.

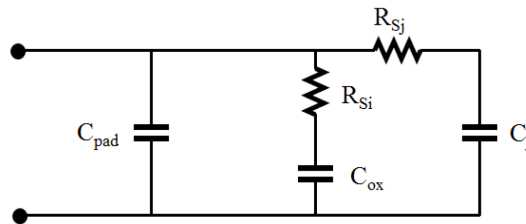

Fig. 7. Small-signal circuit model of a ring modulator.

In order to simulate frequency response of the ring modulators, our model presented in [19] is used. From fitted curves to τ_l versus voltage shown in Fig 4(a), $\frac{\partial(1/\tau)}{\partial v}|_{V_{DC}}$ are calculated to be $-4.4 \times 10^8\ 1/s/V$, $-2.4 \times 10^8\ 1/s/V$, and $-2.6 \times 10^8\ 1/s/V$ for Rings B-D, respectively when $V_{DC} = -1V$. Moreover, from fitted quadratic curves to Δn_{eff} as a function of voltage in Fig. 4(c), $\frac{\partial n_{eff}}{\partial v}|_{V_{DC}}$ are calculated to be $1.88\times10^{-5}\ 1/V$, $1.95\times10^{-5}\ 1/V$, and $2.38\times10^{-5}\ 1/V$ for Rings B-D, respectively. Using the electrical circuit model of ring modulators together with optical parameters listed above, the small-signal electro/optical responses of Rings B-D at various laser wavelength detunings with respect to resonance wavelength ($\Delta\lambda$) are simulated. The results of this simulation at several negative and positive detunings are shown with lines in Figs. 9(a) and 9(b) for Ring B, Figs. 9(c) and 9(d) for Ring C, and Figs. 9(e) and 9(f) for Ring

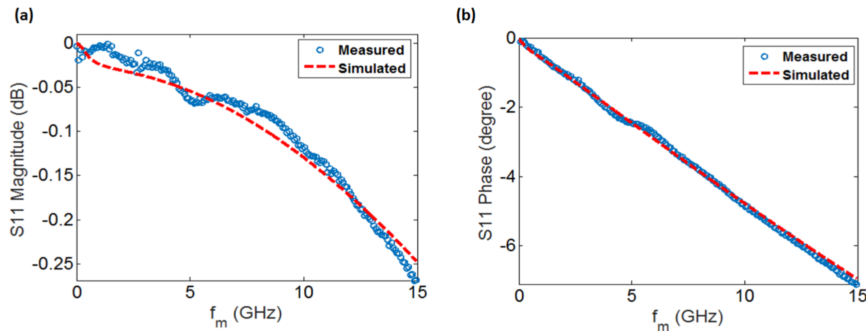

Fig. 8. Measured and simulated electrical S11 (a) magnitude (b) phase of Ring D with $d_{++} = 800nm$.

D. Each curve is normalized to its value at 200MHz.

Frequency response of the ring modulators are measured by a 20GHz lightwave component analyzer (Agilent 8703A) under -1V bias voltage through the full spectrum range of interest. The RF signal is fed to the device using high speed SG probe. All the RF components such as cables, connectors, the RF probe, and a bias tee are de-embedded from the frequency response. A Tunable laser source is coupled to the devices by a fiber grating coupler. The temperature of the stage is kept constant at $25°C$. In order to perform an error-free measurement of the small-signal frequency response at both positive and negative detunings, either the output power should be low to avoid a self-heating effect, or else we should calibrate the measured results to remove the self-heating effects [15]. The laser output power is kept at -7dBm and -10dBm for Rings C and D in order to avoid self-heating. For Ring C, due to higher intrinsic loss, the smaller slope of the spectrum, and the sensitivity limitation of the optical receiver, the measurement results at low input power are noisy. Therefore, we measure the small-signal response of the ring at 6dBm input power and we used the method presented in [15] to remove the effect of self-heating by mapping the measured detuning to real detuning. The measured electro/optical responses (markers) are also added to the simulation results (solid lines) shown in Figs. 9(a) and 9(d). For all three rings at both negative and positive detunings, the measured data are in good agreement with the simulation results. The expected input wavelength-dependent frequency response of the ring modulators [13–15, 19, 28] can be seen from both measurement and simulation results. The difference between frequency responses at positive and negative detunings is a result of loss modulation when modulating the index of the ring resonator [15,19]. Comparing E/O responses of these three rings, the 3dB bandwidth improvements by decreasing d_{++} is clear.

To better quantify the improvement in the device bandwidth, f_{3dB} of rings with various d_{++} versus normalized detuning are calculated based on the small-signal E/O measurements and simulations. Figure 10(a) shows the simulated f_{3dB} as a function of $\Delta\omega\tau$. Measured f_{3dB} are also added for Rings C and D in markers, however, as the minimum bandwidth of Ring B is close to the bandwidth of the lightwave component analyzer, an accurate bandwidth measurement is not possible. Comparing these three rings, the 3dB bandwidth improvements by decreasing d_{++} is obvious. Based on Fig. 10(a), the minimum bandwidth increases from 2.8GHz in Ring D to 17.2GHz in Ring B.

Increasing the laser detuning leads to the bandwidth increase due to the peak generation in the frequency response at high frequencies. However, DC gain, G_{DC}, only rises until a certain detuning (i.e. $\Delta\omega = 1/(\sqrt{3}\tau)$ when neglecting the loss modulation) where beyond this point it decreases [14, 15, 19]. The variation in G_{DC} over laser detuning is quantified by

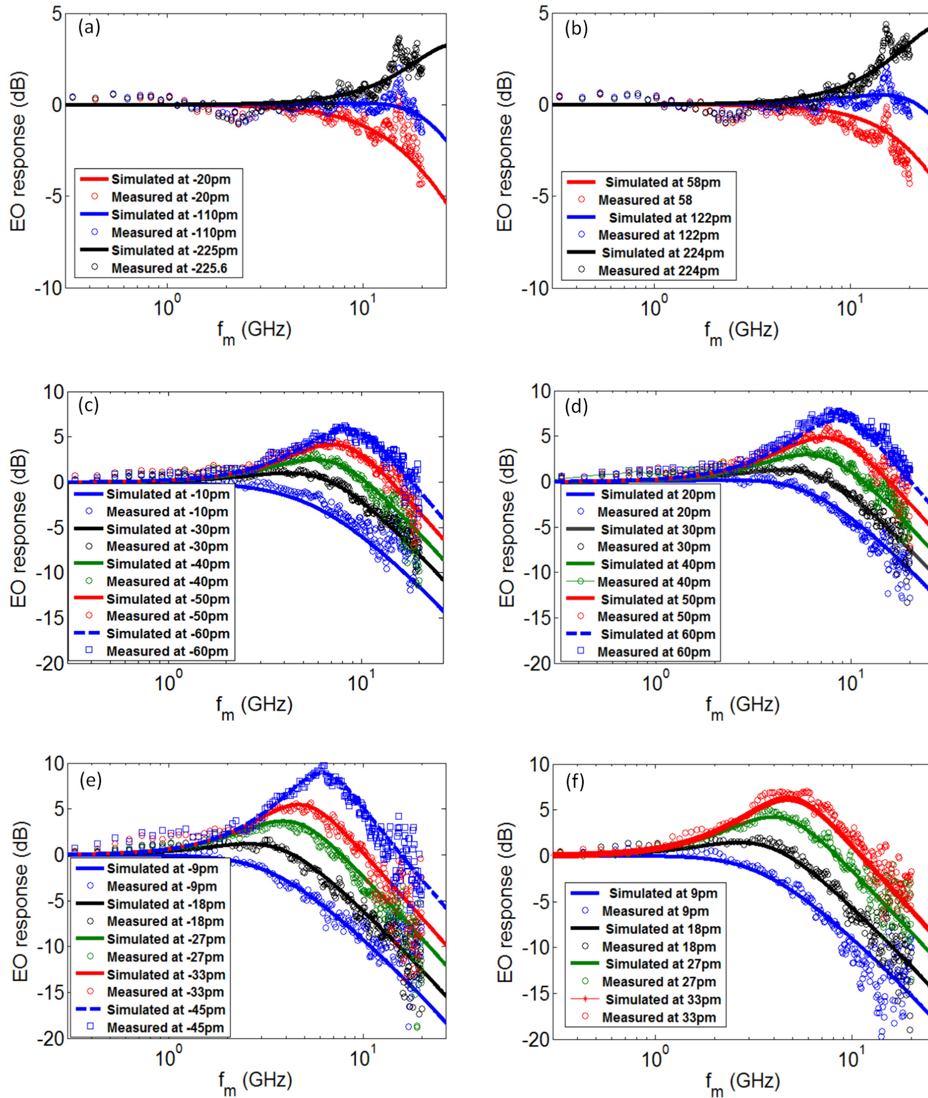

Fig. 9. Simulated (line) and measured (marker) electro/optical response of Ring B with $d_{++} = 350nm$ at (a) negative and (b) positive detunings, Ring C with $d_{++} = 550nm$ at (c) negative and (d) positive detunings, and Ring D with $d_{++} = 800nm$ at (e) negative and (f) positive detunings. Here, f_m is modulation frequency.

G_{DC} penalty, which is essentially G_{DC} at each detuning normalized to the maximum G_{DC} achieved across the entire detuning range [14]. Figure 10(b) shows the simulated penalty in G_{DC} versus normalized frequency detuning, $\Delta\omega\tau$, in a solid line for Ring C. The G_{DC} penalty is similar for all three rings as G_{DC} penalty is only proportional to $\frac{\Delta\omega\tau}{[\Delta\omega^2\tau^2+1]^2}$ [14, 19]. Despite the same G_{DC} penalty, G_{DC} is different for the three ring modulators as each has a different Q, and therefore, a different transmission spectrum slope. Also, from the measured E/O responses shown in Figs. 9(c) and 9(d) at 200MHz, the G_{DC} penalty is calculated and shown with markers in Fig. 10(b) which follows the same trend expected from simulation results. As a reference point, $\pm 60nm$ is equivalent to normalized detuning of around ± 1.72.

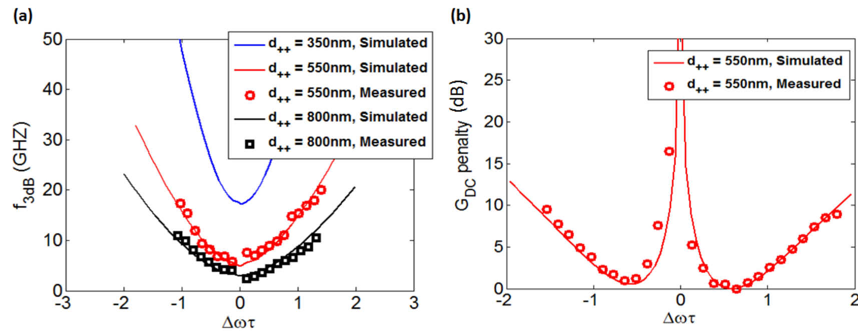

Fig. 10. Simulated (line) and measured (marker) (a) bandwidth of tested ring modulators (b) DC gain penalty of Ring C with $d_{++} = 550nm$ versus $\Delta\omega\tau$.

In [19], we showed that for a non-zero detuning, the ring modulator small-signal electro-optical response has one real pole, one zero, and a pair of complex-conjugate poles. We also showed that the trade-off efficiency between f_{3dB} and G_{DC} penalty rises to a limit when increasing the electrical bandwidth. We assumed that electrical bandwidth only affects the location of the real pole and does not change the locations of zero and complex-conjugate poles. Here, increasing f_{RC} is done through decreasing d_{++} which also alters the optical behavior of the ring modulators. To make this clearer, pole-zero diagrams of Rings B-D are shown in Fig. 11. In this figure, $1/(R_{eqX}C_{eqX})$ ($X = B, C$, and D) shows the pole representing the electrical behavior of the ring modulator while a complex pole located at $-1/\tau_X \pm j\Delta\omega_X$ and a real zero show the optical behavior of the ring modulator. The location of the zero with respect to a complex pole pair depends on the coupling condition [19]. As shown in Fig. 11, all the pole and zero locations are affected by d_{++}. As the quality factor and therefore τ are different in the three rings studied here, we compare ring modulator responses at similar normalized detunings (similar $\Delta\omega\tau$) throughout the paper. This is indicated as a dashed line in Fig. 11 along which the damping factor ($\zeta = 1/\sqrt{1 + (\tau\Delta\omega)^2}$) is similar in Rings B-D while the natural frequency ($\omega_n = \sqrt{\Delta\omega^2 + \frac{1}{\tau^2}}$) of Ring B is higher than Rings C and D.

To study and compare the aforementioned trade-off efficiency, simulated f_{3dB} are plotted versus the G_{DC} penalty in Fig. 12(a) for positive $\Delta\omega$. According to this figure, smaller d_{++} not only results in a higher bandwidth but also results in a more efficient trade-off between the G_{DC} penalty and f_{3dB}. Consequently, d_{++} is shown to be a design parameter in tuning the efficiency of the bandwidth and low frequency eye opening of the ring modulators.

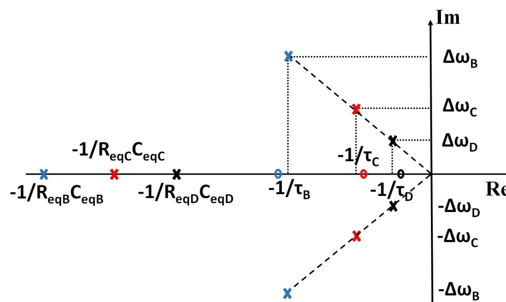

Fig. 11. Pole-zero diagrams of Rings B-D.

The gain-bandwidth product (GBW), defined as $G_{DC} \times f_{3dB}$, for these three rings are plotted in Fig. 12(b). This shows that, although Ring D has the lowest bandwidth, the GBW of Ring D is the highest compared to the other two rings due to its steeper transmission spectra.

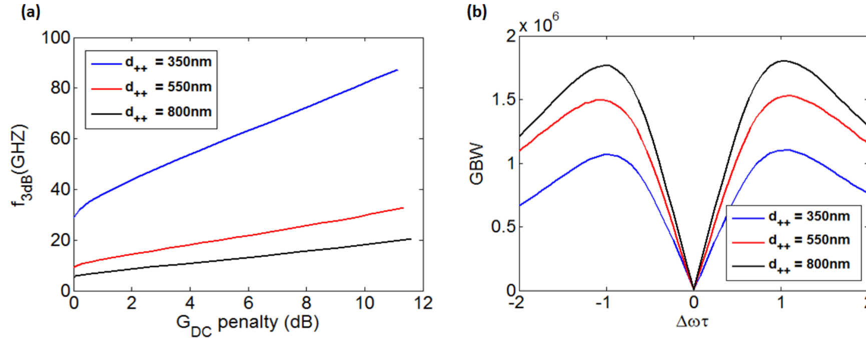

Fig. 12. Simulated (a) f_{3dB} versus DC gain penalty and (b) GBW versus $\Delta\omega\tau$ at -1V bias voltage for Ring B, C, and D with $d_{++} = 350nm$, $d_{++} = 550nm$, and $d_{++} = 800nm$, respectively.

Table 2 summarizes the comparison between Rings B, C, and D in terms of f_Q, f_{RC}, f_{3dB}, maximum GBW, and trade-off efficiency between f_{3dB} and the G_{DC} penalty. The latter is defined as the slope of a fitted line to plots shown in Fig. 12(a). As shown in this table, in terms of the bandwidth, Ring B with the smallest d_{++} among all the rings, has both higher optical, electrical, and consequently total bandwidth. Also, it has the most efficient trade-off between bandwidth and DC gain. However, Ring D, with largest d_{++}, has the highest GBW.

Table 2. Summary of bandwidth, GBW, and f_{3dB}-G_{DC} penalty trade-off efficiency.

Ring	d_{++}(nm)	f_Q(GHz)	f_{RC}(GHz)	f_{3dB}(GHz) @ GBW_{max}	GBW_{max}	f_{3dB}-G_{DC} penalty trade-off efficiency
Ring B	350	39.6	75	44.9	1.1×10^6	5
Ring C	550	9.8	58	15.7	1.5×10^6	2
Ring D	800	5.7	51	10.5	1.8×10^6	1.3

5. Discussions

Above we quantify variations the optical behavior of the device and electrical characteristics of the ring modulators when decreasing d_{++}. In order to assess the ring modulator performance, metrics such as ER and IL should be taken into account in addition to the small-signal frequency response. Although the static ER of the ring modulator may degrade when driven at high frequency, it could still be used as a parameter to compare different ring modulator efficiencies.

As shown in Figs. 5(a) and 5(b), by increasing the detuning on the positive side, ER decreases as the transmitted power at bit 0 and 1 become closer but IL decreases as going farther from the resonance frequency. Also, base on Fig. 6(a), decreasing d_{++} decreases the maximum achievable ER over various applied voltages. At the same time, according to Fig. 6(b), this increases IL. On the other hand, based on Figs. 9(a) and 9(d) and 10(a), the bandwidth of the ring modulator increases significantly by decreasing d_{++}. The three metrics of ER, IL, and f_{3dB} are dependent on laser frequency detuning. According to Fig. 5(a), increasing laser detuning beyond the detuning corresponding to maximum ER, results in decreasing ER while based on Fig. 10(a), it leads to an increase in f_{3dB}. Hence, there will be a trade-off between ER and f_{3dB}

Optics EXPRESS

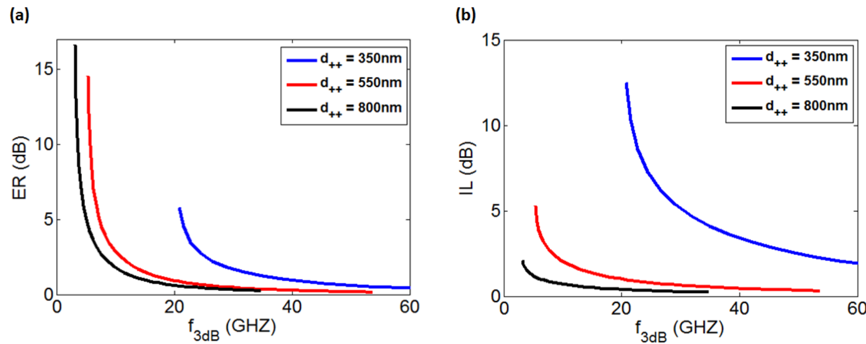

Fig. 13. (a) Extinction ratio and (b) IL versus f_{3dB} for Ring B, C, and D with $d_{++} = 350nm$, $d_{++} = 550nm$, and $d_{++} = 800nm$, respectively.

over laser detuning. Another important parameter is the applied voltage which determines ER and IL (Figs. 6(a) and 6(b)).

In order to see these relations between ER and IL with f_{3dB} more clearly, Figs. 13(a) and 13(b), plot the ER and IL obtained from measured transmission spectra with voltages varying between 0-4V as a function of f_{3dB} computed at 0V. Here, we consider positive frequency detunings. According to Fig. 13(a), ER above 5.7dB is not achievable for Ring B. Also, considering ER above 4dB, the maximum f_{3dB} achievable for Rings B, C, and D are 22.1GHz, 8.2GHz, and 5.8GHz, respectively. The minimum IL corresponding to these maximum f_{3dB} from Fig. 13(b) are 9.4dB, 2.5dB, and 1dB for Ring B, C, and D, respectively. These values are summarized in Table 3 together with the corresponding detunings. Also, the corresponding TP values are included in the table showing that Ring B has a TP value that is 7.7dB higher than that of Ring D. At applied voltage of 4V, to achieve 4dB ER, the bandwidth can increase by 3.8× by decreasing d_{++} from 800nm to 350nm but at the price of 8.4dB extra IL. Please note that ER and IL reported here are calculated based on DC measurement, and could be an overestimation of the values measured at large signal domain depending on the operating bit rate.

Table 3. Comparison between ring modulators in terms of ER, IL, TP, and f_{3dB} at 4V applied voltage.

Ring	d_{++}(nm)	ER(dB)	IL(dB)	TP(dB)	f_{3dB}(GHz)	$\Delta\omega\tau$
Ring B	350	4	9.4	14	22.1	0.4
Ring C	550	4	2.5	7.7	8.2	0.52
Ring D	800	4	1	6.3	5.8	0.66

Figures 14(a) and 14(b) show f_{3dB} and IL versus d_{++} for targeted $ER = 4dB$ and $ER = 5dB$, respectively, at 4V applied voltage. The rate of change over d_{++} is different for f_{3dB} and IL. At $ER = 4dB$, increasing d_{++} from 350nm to 550nm and from 550nm to 800nm, decreases f_{3dB} by 0.37× and 0.7×, respectively, while IL decreases around 0.49×, in linear scales, for both cases. These rates of change are similar when $ER = 5dB$. As the rates of change in IL and f_{3dB} are different, depending on the importance of f_{3dB} and IL, the definition for figure of merit may vary. For example, in some applications bandwidth of the device is more important and a few dB extra IL is acceptable within the link budget. In that case, in the defined figure of merit, there should be a higher weight for f_{3dB} compared to IL which may result in selecting a smaller d_{++}. In this study, we selected a wide range of d_{++} values to observe the trend of variation in parameters such as loss, IL, f_{RC}, f_Q, and f_{3dB}. Based on this study, for small values of d_{++} (350nm and 200nm), an exponential increase in loss by decreasing d_{++} (Fig. 4(b)) results in the

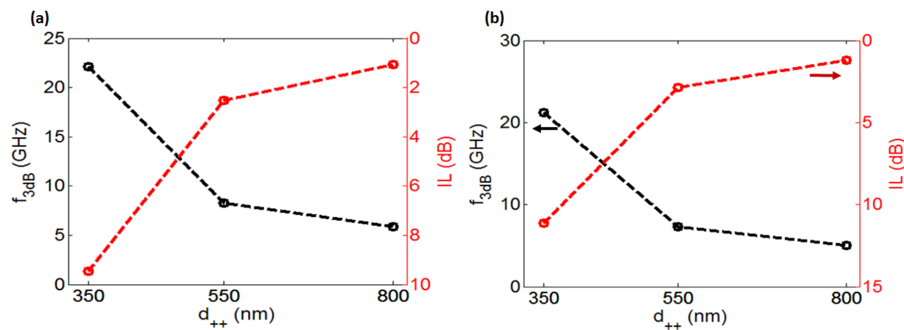

Fig. 14. Bandwidth and IL versus d_{++} for (a) $ER = 4dB$ and (b) $ER = 5dB$ at 4V applied voltage.

photon lifetime, τ_l, to be the main reason in improvement of bandwidth rather than electrical bandwidth. This has a disadvantage of an increase in IL. If IL needs to be kept in a certain range, then based on the trend of variation in τ_l and R_{sj} given here, d_{++} can be selected accordingly. On the other hand, aside from the rise in IL, a decrease in the ring quality factor at smaller d_{++} values increases the tolerance of the resonance wavelength walk-off and , therefore, relaxes the control feedback loop design [4].

Fabrication tolerance is also an important factor, especially for the small d_{++} values. The doping implantation usually has a few tens of nm offset. Due to the exponential increase in loss by decreasing d_{++} (Fig. 4(b)), at small d_{++} values this will increase the fabrication sensitivity. Selecting the right value for d_{++} depends on the link power budget, the required bandwidth, the available peak-to-peak voltage at the driver, the required ER, and process tolerance.

Also, here we considered symmetric positioning of the high doped regions as it is the most common configuration. However, d_{++} could be asymmetric in order to add an extra handle for further optimization of the ring modulator performance. This is due to different carrier absorption of electrons and holes [21] as well as the longer interaction length of optical mode with the outer side of the ring modulator than the inner side. Therefore, asymmetric d_{++} could be helpful to decreasing the insertion loss while maintaining the same electrical bandwidth. Another way of improving of the ring performance is to add intermediate doping together with the optimized d_{++}. This will help decreasing the series resistance and hence improving the bandwidth while not inducing too much loss on the ring modulator.

6. Conclusions

We performed DC and small-signal simulations and measurements of reverse-biased ring modulators fabricated in IME A*Star process with various high-doped region locations of 200nm, 350nm, 550nm, and 800nm distance from the edge of the waveguide. The model for small-signal frequency response of the ring modulator presented before is used to provide further insight into the device design and optimization. Based on the DC and AC characteristics of the devices, we assessed optical and electrical properties of the ring modulators based on the location of the high-doped region. Parameters such as additional loss, ER, IL, TP, and optical and electrical bandwidths were compared among various ring modulators.

Acknowledgment

Authors are grateful for the financial support of the Natural Sciences and Engineering Research Council of Canada and Ontario Centres for Excellence.